

# SPHERICAL PARTICLE MIGRATION EVALUATION IN LOW REYNOLDS NUMBER COUETTE FLOW USING SMOOTH PROFILE METHOD

MAHYAR POURGHASEMI<sup>1</sup>, NIMA FATHI<sup>1</sup>, PETER VOROBIEFF<sup>1</sup>, GOODARZ AHMADI<sup>2</sup>, SEYED SOBHAN ALEYASIN<sup>3</sup> & LUIS EÇA<sup>4</sup>

<sup>1</sup> Mechanical Engineering Department, University of New Mexico, Albuquerque, NM, USA.

<sup>2</sup> Mechanical and Aeronautical Engineering Department, Clarkson University, Potsdam, NY, USA.

<sup>3</sup> Department of Civil and Environmental Engineering, University of Windsor, Windsor, Ontario, Canada.

<sup>4</sup> Mechanical Engineering Department, Instituto Superior Técnico, Lisbon, Portugal.

## ABSTRACT

An Eulerian–Lagrangian model is developed to investigate the solid particle migration in low Reynolds number shear flows between two parallel plates. A continuous kernel function with a predefined thickness is applied in the implemented numerical model to smooth the discontinuity at the interface between primary and secondary phases. At each time step, the solid particle's rotation and displacement are calculated to directly capture the interaction between the solid particle and primary liquid phase without simplification. Solution verification is performed using the global deviation grid convergence index approach. The observed order of accuracy for the primary phase solver approaches 2, consistent with the formal order of accuracy of the applied discretization scheme. The obtained velocity profiles from the implemented numerical approach show a good agreement with the analytical solution, confirming the single-phase flow solver's reliability. The obtained numerical results from the applied Eulerian–Lagrangian multiphase model are also compared with experimental data from a linear shear flow apparatus with suspended buoyant particles, and good agreement was found.

**Keywords:** CFD, multiphase flow, particle migration, shear flow, solid–fluid interaction, verification and validation.

## 1 INTRODUCTION

Solid–liquid multiphase flow analysis is an interdisciplinary research area with various technological applications. From the sediment transport in rivers, fillers motion within polymers, to high-performance coolants, having a correct understanding of particle–fluid flow interactions plays a key role in research and development. Fluid flows containing small-size particles occur in biological and engineering systems, including aerosol transport, air pollution, paper-making, and targeted drug delivery processes. Analyzing fluid flow with suspended particles is important not only for predicting the motion of particles within the primary fluid phase but also for evaluating their impact on the flow of the primary phase. Computational methods have been developed to analyze and evaluate the multiphase flow in different scales. Multiphase flow modeling using computational fluid dynamics goes back to the 1950s and the 1960s when Particle-in-Cell (PIC) and Marker-and-Cell (MAC) methods were developed at Los Alamos National Laboratories [1–4]. A recent review of the MAC method can be found in McKee et al. [5]. Although the MAC method provided significant progress in numerical modeling of the multiphase flows, it was relatively inaccurate. The volume of fluid (VOF),

front tracking, as well as level set methods, were more robust and accurate techniques proposed in the late 1980s to investigate multiphase flows numerically [6–8]. The VOF approach uses a color/marker function representing the phase fraction of each fluid within a computational cell. The main problem with the VOF method is capturing the sharp boundary between different phases and interfacial properties such as surface curvature and surface tension [9]. Front Tracking Method introduced in the late eighties uses the Eulerian approach to solve a single set of governing equations, that is, Navier–Stokes and continuity equations for incompressible fluid flow, in the entire computational domain. Sharp changes in material properties such as viscosity and density can be captured, while the effect of surface tension is included by adding an appropriate source term at the interface between different phases in the front tracking technique [10]. The interface is directly captured by tracking the marker points on the boundaries between different phases. The direct representation of the boundaries between different fluids makes this method suitable and accurate to investigate and capture interfacial phenomena such as surface tension, force balance, phase change, and surface curvature with a high order of accuracy. Recently, other analytical and computational investigations were performed on particle–fluid interaction. Ingber et al. [11] evaluated different particle interactions, including particle/particle, wall/particle, and particle migration, in different types of nonlinear shear fields. A semi-analytical solution was developed for the motion of two spherical particles suspended in an unbounded arbitrary shear flow by the same group [12]. The results of the discrete phase element method (DPM) against the analytical solution were evaluated, and the verification and validation (V&V) for the single and double particle trajectories in a rectangular and cylindrical domain were conducted in [13–16]. Previously, our progress on applying the DPM using the ANSYS/Fluent code to model the particle migration was reported in [17]. The current investigation is dedicated to studying the particle behavior in a low Reynolds number Couette shear fluid flow under different boundary conditions using our recently developed Eulerian–Lagrangian computational code using a similar scheme as the smooth profile (SP) method [18, 19] to simulate the coupled solid and fluid phases simultaneously.

## 2 NUMERICAL APPROACH

A finite volume CFD code has been developed to study the migration of a solid particle in low Reynolds number Couette flows between two parallel plates. Figure 1 shows the computational domain used in the numerical simulations. The left and right boundaries are assigned as a periodic boundary condition.

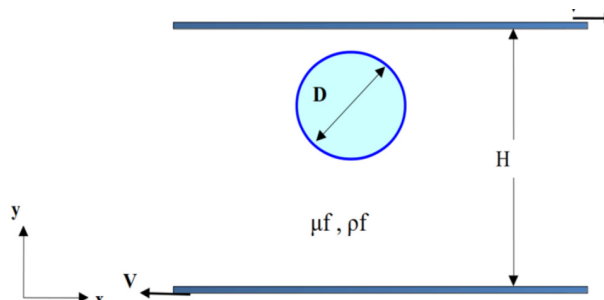


Figure 1: Schematic illustration of the motion domain of a suspended particle in a 2-D Couette flow.

The incompressible Navier–Stokes (N–S) equation is given as follows:

$$\frac{\partial(\rho_f u_f)}{\partial t} + \nabla \cdot (\rho_f u_f u_f) = -\nabla P + \nabla \cdot [\mu_f (\nabla u_f + \nabla u_f^T)], \quad (1)$$

where  $u_f$  is the fluid velocity,  $P$  is the relative pressure with the hydrostatic pressure as the reference, and  $\rho_f$  and  $\mu_f$  are the density and viscosity of the fluid phase, respectively. Since the fluid is assumed to be incompressible, the continuity equation simplifies to the following:

$$\nabla \cdot u_f = 0. \quad (2)$$

The translational and rotational motions of the solid particle within the flow field are considered using the Lagrangian approach. These are as follows:

$$\begin{aligned} m_s \frac{du_s}{dt} &= F_f + F_b \\ I_s \frac{d\omega}{dt} &= T_f, \end{aligned} \quad (3)$$

where  $m_s$  is the particle mass,  $u_s$  is the particle velocity,  $F_f$  is the hydrodynamic force imposed by the fluid on the particle, and  $F_b$  is the buoyancy force acting on the spherical particle. Also,  $I_s$  is the rotational inertia of the particle,  $\omega$  is the particle angular velocity, and  $T_f$  is the torque inserted by the fluid to the particle at the interface. The hydrodynamic force and torque exerted by the fluid flow on the solid particle are given in eqn (4):

$$\begin{aligned} F_f &= \oint_{interface} \{-P + \mu_f (\nabla u_f + \nabla u_f^T)\} \cdot dl \\ T_f &= \oint_{interface} r \times \left[ \{-P + \mu_f (\nabla u_f + \nabla u_f^T)\} \cdot dl \right] \end{aligned} \quad (4)$$

To overcome discontinuity at the interface in this Eulerian–Lagrangian approach, the interface between solid particle and primary fluid phase is replaced by a kernel function,  $\psi$ , creating a SP from solid into the liquid with a predefined thickness [1,2]. The only input parameter for this smoothed kernel function is the thickness of the interface,  $\delta$ . The corresponding kernel function for the smoothed profile that is used in the present work is given by [2] as follows:

$$\begin{aligned} \psi(x) &= f(|x - x_c|) \\ f(x) &= \frac{G(r + \delta/2 - x)}{G(r + \delta/2 - x) + G(x + \delta/2 - r)} \\ G(x) &= \begin{cases} \exp\left(\frac{dx^2}{x^2}\right) & x \geq 0 \\ 0 & x < 0 \end{cases}, \end{aligned} \quad (5)$$

where  $r$  is the radius of the particle,  $x_c$  is the particle's center of mass,  $dx$  is the spatial discretization size, and  $\delta$  is the interface thickness, which is the only input parameter to define the smoothing kernel function. As it can be inferred from eqn (5), the kernel function  $\psi$  is 1 within the solid particle region,  $|x - x_c| < (r - \delta/2)$ , zero in the fluid region,  $|x - x_c| > (r + \delta/2)$ ,

while varying smoothly from 1 to 0 within the interface thickness. Using the kernel function, the velocity field in the entire solution domain can be expressed as follows:

$$u = (1 - \psi) u_f + \psi u_s, \quad (6)$$

where  $u_s$  designates the velocity of the solid particle. With a well-defined time step and initial velocities within solid and fluid domains, eqns (1–6) are solved numerically using the smoothed profile method proposed by Nakayama and Yamamoto [16, 17]. The finite volume technique is applied to the N-S equations along with the continuity equation, given by (1) and (2). The derived system of equations is solved simultaneously to obtain fluid velocity distribution as well as pressure field with the use of an explicit second-order projection method [19,20] using spatially central-difference approximation on a fixed, staggered grid configuration. Obtained results are considered as intermediate velocity and pressure fields ( $u_f^*$ ,  $P_c^*$ ). Total velocity is equal to the velocity of the particle within the particle domain,  $|x - x_c| < (r - \delta/2)$ .

At the interface, due to the no-slip boundary condition, the velocity of both phases is equal. These two constraints are applied by correcting the intermediate pressure and velocity fields. The corrected pressure field,  $P_c$  and fluid velocity are used to study the disturbing effect of the solid particle on the fluid velocity field.

$$(1 - \psi) u_f = (1 - \psi) u_f^* - \frac{\nabla P_c}{\rho_f} dx. \quad (7)$$

The total velocity field defined in eqn (6) should be divergence-free. By taking the divergence of eqn (6) and considering eqn (7), the Poisson equation for the correction pressure field is derived as follows:

$$\begin{aligned} \nabla^2 P_c &= \frac{\rho_f \nabla \cdot \{ \psi (u_s - u_f^*) \}}{dx} \\ P &= P^* + P_c \\ u &= u_f^* + \psi (u_s - u_f^*) - \frac{\nabla P_c}{\rho_f} dx. \end{aligned} \quad (8)$$

Consequently, eqn (4) converts to the following equation:

$$\begin{aligned} F_f &= - \int \{ \rho_f \psi (u_s - u_f^*) / dx - \nabla P_c \} d\forall \\ T_f &= - \int \rho_f (x - x_c) \times \{ \psi (u_s - u_f^*) / dx - \nabla P_c / \rho_f \} d\forall \end{aligned} \quad (9)$$

After obtaining the hydrodynamic force and torque, particle translational and angular velocities are updated using eqn (3). This procedure repeats for the next time step.

### 3 EXPERIMENTAL APPROACH

The initial motivation was to develop a new particle model originated from our experimental analyses, which have been conducted for several years. Figure 2 shows the experimental setup. As can be seen, the experimental setup consists of a tank and a computer-controlled stepper motor (compumotor). The compumotor is used to displace the belts shown in Fig.



Figure 2: The experimental setup used to study the migration of suspended particles.

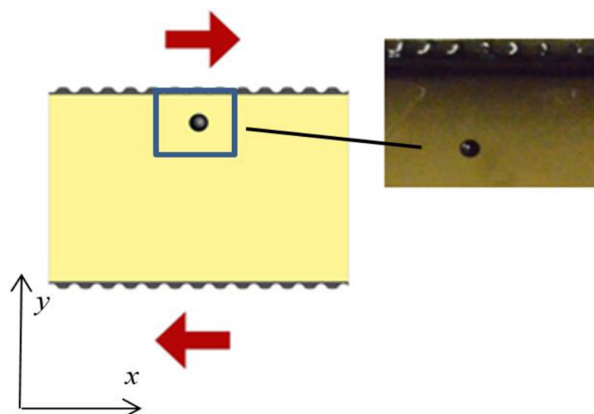


Figure 3: Top view of the single spherical particle and the moving upper belt.

2. In the setup to determine the behavior of a spherical particle suspended in linear shear flow, one spherical polymethyl-metacrylate particle with a diameter of 6.35 mm is suspended between two layers of fluids with approximately equal viscosity and different density. The particle was placed into a tank between two belts, as shown in Fig. 3.

#### 4 RESULTS AND DISCUSSION

To assess the accuracy of the developed CFD code, in the first scenario, a single-phase Couette flow between two parallel plates with a distance of 0.1 m is considered while the top plate moves with a velocity of 1 m/s toward the right and the bottom plate moves with the same velocity in the opposite direction (toward left). The density of the fluid has been considered as  $1 \text{ kg/m}^3$ ,

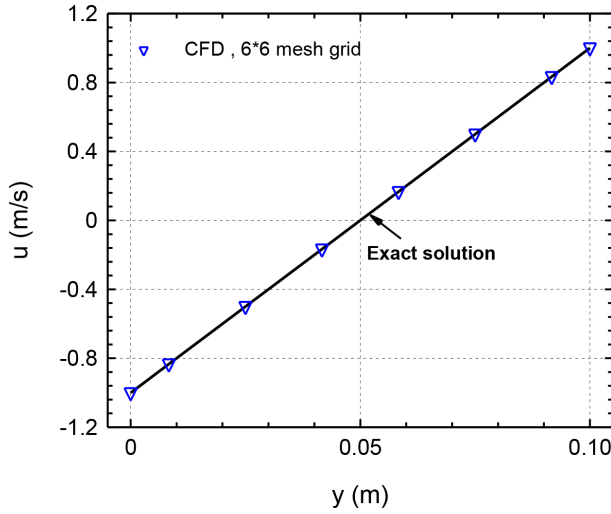


Figure 4: Velocity distribution for Couette flow between two parallel plates, mesh grid of  $6 \times 6$  elements.

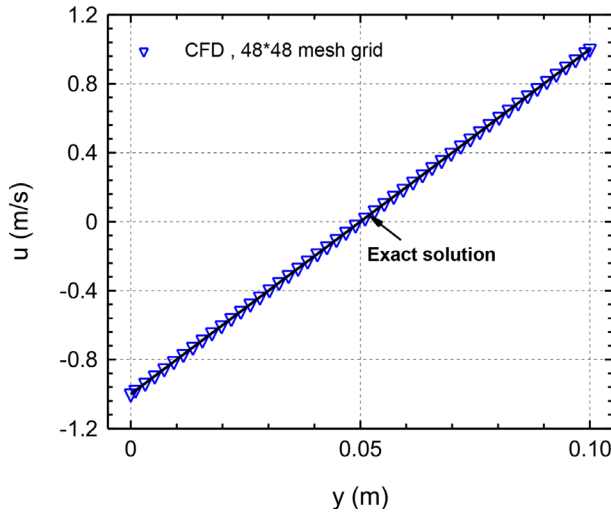


Figure 5: Velocity distribution for Couette flow between two parallel plates, mesh grid of  $48 \times 48$  elements.

and the fluid viscosity is 0.001 Pa. S. The simulations have been conducted for mesh grid sizes of  $3 \times 3$ ,  $6 \times 6$ ,  $12 \times 12$ ,  $24 \times 24$ , and  $48 \times 48$  cells, respectively. Figures 4 and 5 show the numerical results as well as exact solutions for  $u$  velocity in the middle of the domain for a mesh grid of  $6 \times 6$  cells and  $48 \times 48$  cells.

As it can be observed from Figs. 4 and 5, the developed CFD solver gives accurate results even with the coarse mesh of  $6 \times 6$  mesh elements. This is mainly because of the simplicity of the problem since there are no advection and pressure terms, and the flow field is mainly controlled by viscous diffusion.

Table 1:  $L_1$ ,  $L_2$ , and  $L_\infty$  norms for single-phase Couette flow.

Mesh Grid (elements)	$L_1$	$L_2$	$L^\circ$
$3 \times 3$	2.16e-4	2.64e-4	3.23e-4
$6 \times 6$	9.83e-6	1.04e-5	1.47e-5
$12 \times 12$	3.98e-6	4.37e-6	5.97e-6
$24 \times 24$	3.14e-6	3.48e-6	4.88e-6
$48 \times 48$	2.97e-6	3.3e-6	4.65e-6

The  $L_1$ ,  $L_2$ , and  $L_\infty$  norms for single-phase Couette flow are presented in Table 1 in order to investigate the observed order of accuracy of the implemented CFD solver. Figure 6 also shows the obtained observed order of accuracy.

As shown in Table 1 and Fig. 6, the observed order of accuracy is 4.5 for a mesh grid of  $6 \times 6$  elements, and then decreases to 1.5 for a mesh grid of  $12 \times 12$  elements, while it reaches 0.1 for a mesh grid of  $48 \times 48$  elements. The formal order of accuracy is 2, both for spatial and temporal variables. This observed order of accuracy seems strange, while it reduces continuously by mesh refinement.

The exact solution of this flow is a straight line, and so the discretization error would be zero if there were no round-off errors and iterative errors. Round-off errors are unavoidable, and the results of Table 1 suggest that single precision was used. It is observed that the summation of truncation and round-off error for this simple flow becomes larger than the discretization error after the mesh grid size of  $6 \times 6$  elements. As a result, the observed order of accuracy reduces continuously with further mesh refinement. Although the observed order of accuracy is less than 2 for Couette flow, Fig. 5 shows that the obtained result for velocity matches very well the exact (analytical) solution for a mesh grid size of  $48 \times 48$  elements.

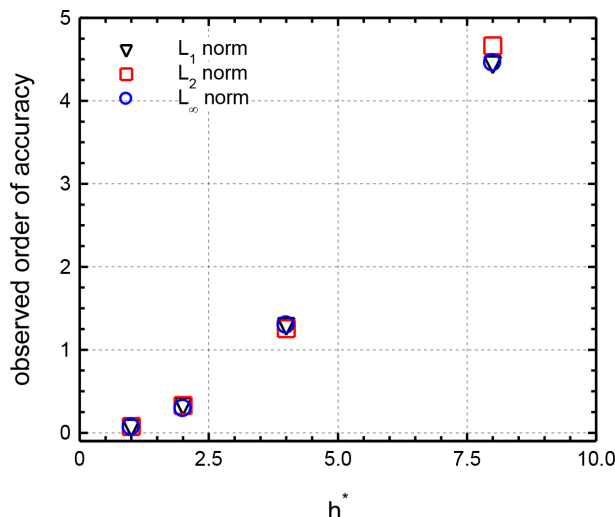


Figure 6: The observed order of accuracy for single-phase Couette flow obtained from results presented Table 1.

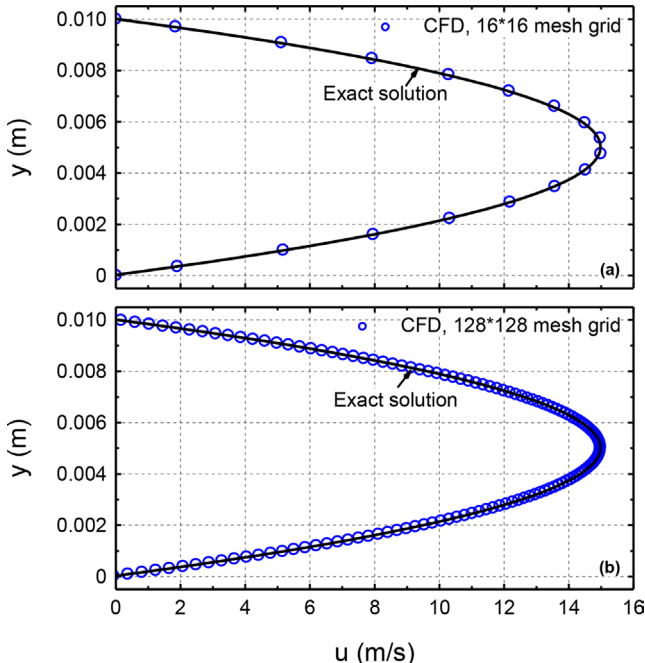


Figure 7: Velocity distribution for a pressure-driven flow between two parallel plates. (a) Mesh grid  $16 \times 16$ ; (b) Mesh grid  $128 \times 128$ .

The second verification scenario for a pressure-driven flow between two parallel plates is considered to further verify the code accuracy. The channel is 0.2 m long and 0.01 m wide with a periodic boundary condition at left and right ends, and an applied pressure gradient of 240 Pa. Fluid density is 1 kg/m<sup>3</sup>, and its viscosity is 0.001 Pa.S. Numerical simulations have been conducted for grid sizes of  $8 \times 8$ ,  $16 \times 16$ ,  $32 \times 32$ ,  $64 \times 64$ , and  $128 \times 128$  mesh elements.

Figure 7 compares velocity profiles predicted by the present CFD code for the primary phase with mesh grids of  $16 \times 16$  and  $128 \times 128$  elements with the exact solution. The CFD results match the exact solution fairly well, confirming the accuracy of the single-phase flow solver. Since the primary phase is a fully developed flow (solution does not change in the x-direction), the error was calculated along the y-direction. Note that the errors were calculated for cross-sections of the domain and they differ only at the level of round-off error.

The observed order of accuracy from the CFD results of a pressure-driven flow between two parallel plates for different norms is presented in Fig. 8. As can be seen, the observed order of accuracy for the developed Fortran CFD code approaches the formal order of accuracy, which is 2. In contrast with the single-phase Couette flow, pressure and viscous terms affect the flow field in this simulation scenario. The truncation and round off errors are much smaller than discretization error, and therefore, the observed order of accuracy is 2, which is consistent with the formal order of accuracy of the applied numerical algorithm in the developed code.

The migration of a solid particle in a Couette flow is studied. The above-mentioned periodic and the no-slip wall boundary conditions in the x- and y-direction, respectively, are used (Fig. 3). The following nondimensional numbers are also used in the study:

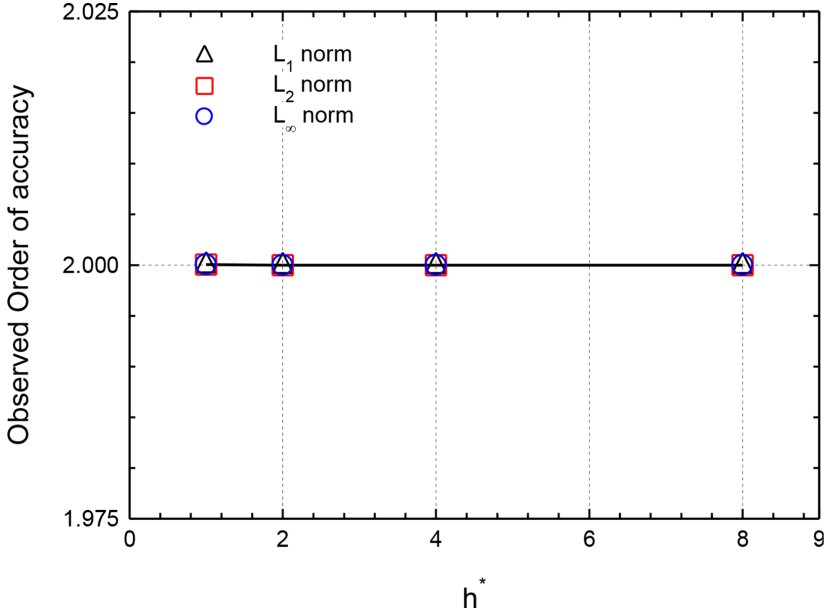


Figure 8: Observed order of accuracy for the pressure-driven flow.

$$\alpha = \frac{\rho_f}{\rho_s}; \quad \zeta = \frac{D}{H}; \quad \text{Re} = \frac{2\rho_f VH}{\mu_f}, \quad (10)$$

where  $D$  is the particle diameter,  $H$  is the distance between two parallel walls in the Couette flow, and  $V$  is the velocity magnitude of the upper and lower walls. Table 2 summarizes the corresponding nondimensional numbers used in this study.

The experimental data on the migration of particles in a low Reynolds number Couette flow from our experimental setup was used to perform validation. The top belt moves with a velocity of 0.002 m/s to the left, while the bottom belt moves with the same velocity to the right. The particle is initially located near the top belt, while its center of mass is 1.25  $D$  below the belt. To study the effect of the slip boundary condition, a different set of simulations, including the slip boundary condition instead of no-slip boundary conditions were performed. Slip boundary condition can be modeled numerically using the concept of slip length,  $\beta$  [16]. Slip length measures a distance from the interface where the fluid velocity reaches to zero. Eqn (11) is implemented in the performed numerical simulation in order to find the fluid slip velocity at the walls of the computational domain (see Fig. 1).

$$u_{wall} = \beta \frac{du}{dy} \Big|_{wall} \quad (11)$$

Table 2: Nondimensional numbers used in numerical simulations

$\alpha$	$\zeta$	Re
1	0.0888	0.04–0.32

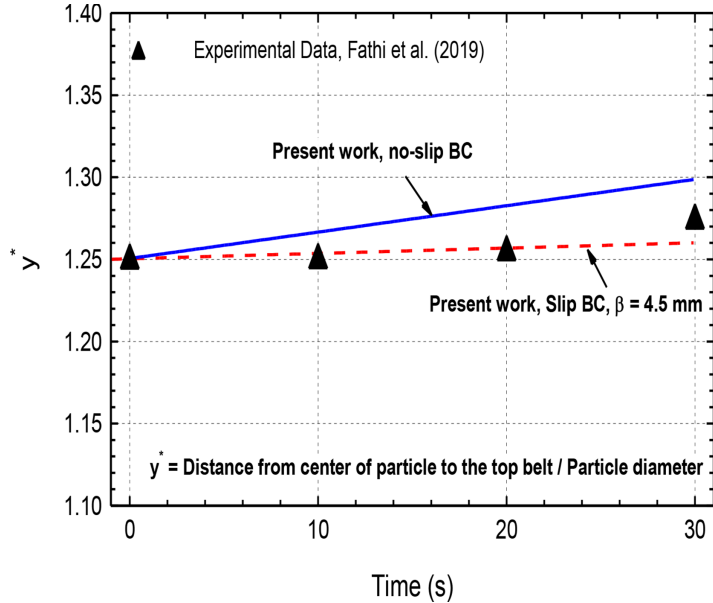


Figure 9: Comparison between the experimental data and numerical results on the migration of solid particles.

Figure 9 compares the experimentally measured and numerical predicted migration rates. It is observed that the particle migrates slowly toward the channel centerline. The migration rate is quite small, and the uncertainty in the experimental data is considerable. However, the CFD prediction and the experimental data follow the same trend. The ratio between the particle's center of mass relative velocity and belt velocity as the applied CFD boundary condition is presented in Fig. 10. It is seen that there is a considerable difference between the

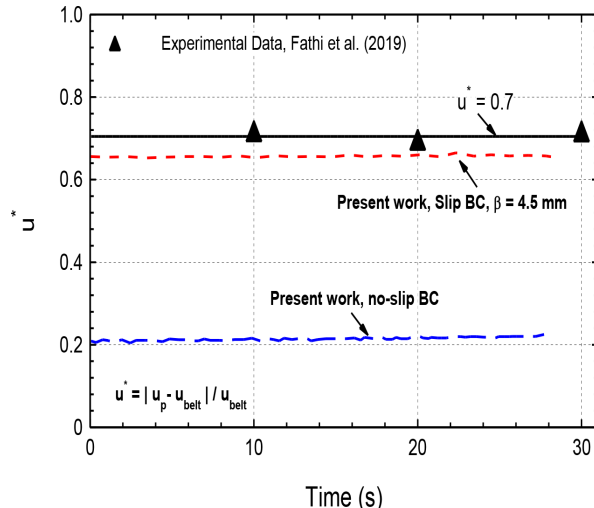


Figure 10: Comparison of the numerical results on the particle relative velocity with the experimental data.

experimental data and the CFD prediction for the case with no-slip boundary condition. The CFD result with a no-slip boundary condition at the belts suggests that the relative velocity ratio is around 0.21, while experimental data gives a value of 0.7.

In the performed numerical simulations with the no-slip boundary condition for the walls, the velocity profile within the fluid domain is high near the top and bottom belts such that the particle centerline velocity is around 79% of belt velocity, as shown in Fig. 10. However, the velocity ratio obtained from the conducted experiment in Fig. 10 is around 0.3. The deviation between the obtained numerical results and experimental data for the particle centerline velocity illustrated in Fig. 10 is due to fluid slippage at the belts in the experiments.

It is observed in Figs. (9) and (10) that by considering a slip length of 4.5  $\mu\text{m}$ , the velocity ratio and particle migration rate approach to the experimental data. Therefore, the current numerical simulations predict a slip length of 4.5  $\mu\text{m}$  for the fluid near the belts in the performed experiments. Further numerical simulation with an apparent slip length of  $\beta = 4.5 \text{ mm}$  was conducted, and the result is presented in Figs. 9 and 10. It is observed that by considering apparent slip, the velocity ratio and particle migration rate get closer to the experimental data. Further numerical simulations at different Reynolds numbers were performed to investigate the effect of shear rate on particle migration in a Couette flow. Figure 11 presents the trajectory of the center of the mass of the particle as a function of time for different Reynolds numbers of 0.04–0.32. As it is seen, the particle migrates toward the center of the

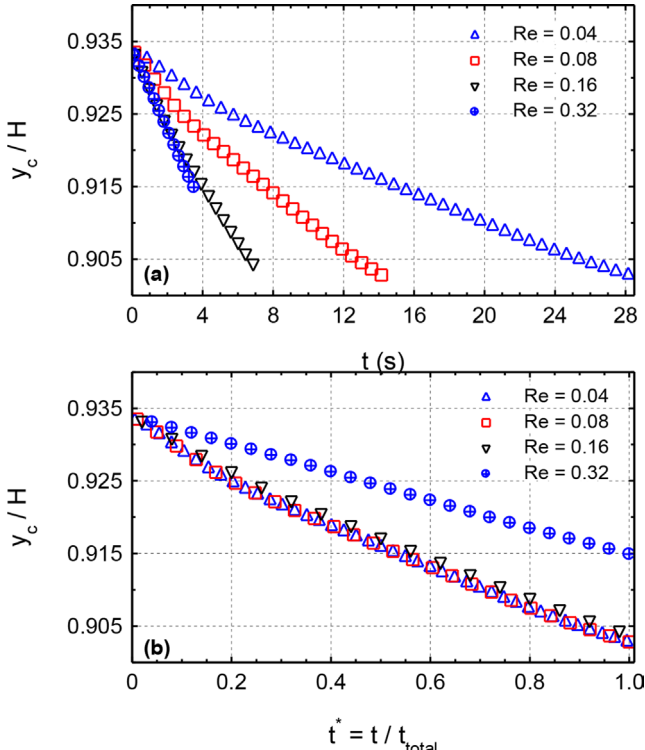


Figure 11: Trajectories of the suspended particle as a function of time for different Reynolds numbers.

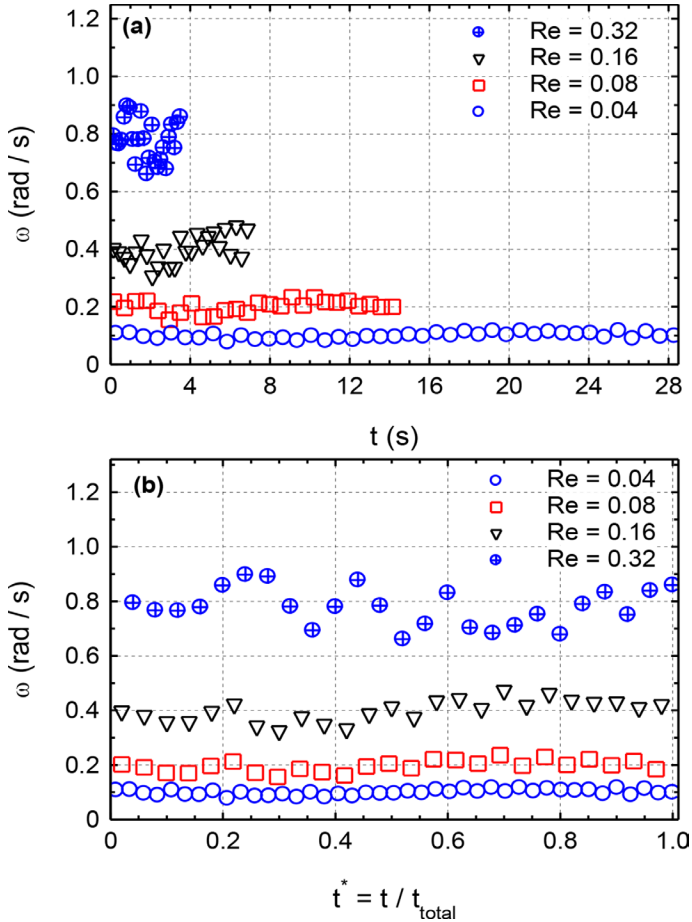


Figure 12: Instantaneous angular velocities of the suspended particle as a function of time for different Reynolds numbers.

flow domain ( $y_c/H = 0.5$ ), where the shear stress is the lowest. The initial position of the solid particle is the same for all Reynolds numbers, and simulations are terminated once the particle leaves the solution domain from left or right boundaries (see Fig. 2). At high Reynolds numbers, the particle travels faster, and therefore, as presented in Fig. 11, the corresponding simulation time is shorter.

The inertial lift force on a migrating particle is exerted within a shear flow. This force is first observed and formulated by Saffman in the 1960s [21]. In this work, the combination of imposed inertia and lift forces from the fluid flow resembles the Saffman lift force and pulls the particle toward the channel centerline, as can be inferred from migration rates in Fig. 12. The streamlines around the particle at Reynolds number of 0.32 are shown in Fig. 13. A counterclockwise rotation of the particle can be observed, which tends to push the particle upward toward the top plate.

Figure 14 illustrates the angular velocity of the particle as a function of time for the Reynolds number in the range of 0.04–0.32. Angular velocity increases as the Reynolds number

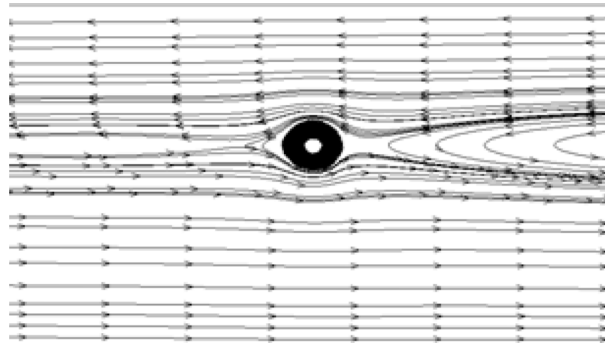


Figure 13: Streamlines around the solid sphere in Couette flow with the Reynolds number of 0.32.

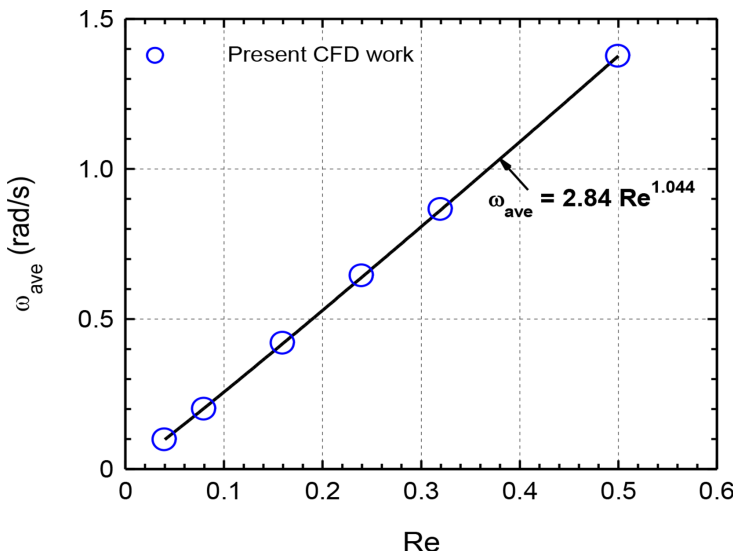


Figure 14: Average particle angular velocity as a function of Reynolds number.

gets higher, and so does the fluid velocity near the particle surface. However, the observed trend for particle migration rate in Fig. 11 suggests that the inertia force from fluid flow dominates in the case of low Reynolds number Couette flow ( $Re < 0.32$ ) and, therefore, particle migrates toward the centreline. The average angular velocity correlates with the Reynolds number and can be fitted to eqn (12):

$$\omega_{ave} = 2.84 Re^{1.044}. \quad (12)$$

As it can be inferred from Fig. 14 and eqn (12), in the low Reynolds number Couette flow ( $Re < 0.32$ ), the induced angular velocity of the particle varies almost linearly with the Reynolds number.

## 5 CONCLUSIONS

The results of the newly developed Eulerian–Lagrangian model for a spherical single-particle migration in a low Reynolds number shear flow were presented. Code verification and solution verification were conducted for the primary phase. The solid particle (secondary phase) migration was evaluated by performing validation against the experimental data obtained from our low Reynolds apparatus. The obtained computational results of the solid particle migration rate and relative transport velocity showed good agreement with the experimental data confirming the accuracy and reliability of the Eulerian–Lagrangian approach. It was observed that the solid particle tends to migrate toward the channel centerline at all Reynolds numbers (0.04–0.32). The obtained induced average angular velocity of the solid particle was observed to vary almost linearly with the Reynolds number.

## ACKNOWLEDGMENTS

The experimental apparatus used in this study was originally developed with funding from the National Science Foundation (Grant 1335907).

## REFERENCES

- [1] Evans, M.W. & Harlow F.H., 1957, *The Particle-in-Cell Method for Hydrodynamic Calculations*. Los Alamos National Laboratory Report LA-2139.
- [2] Harlow, F., Hydrodynamic problems involving large fluid distortion. *Journal of ACM*, **4**, p. 137, 1957. <https://doi.org/10.1145/320868.320871>
- [3] Harlow, F. & Welch, J.E., Numerical calculation of time-dependent viscous incompressible flow of fluid with a free surface. *Physics of Fluids*, **8**, pp. 2182–2189, 1965. <https://doi.org/10.1063/1.1761178>
- [4] Yoo, J.Y., & Na, Y., A numerical study of the planar contraction flow of a viscoelastic fluid using the simpler algorithm. *Journal of Non-Newtonian Fluid Mechanics*, **30**, pp. 89–106, 1991. [https://doi.org/10.1016/0377-0257\(91\)80005-5](https://doi.org/10.1016/0377-0257(91)80005-5)
- [5] McKee, S., Tome, M.F., Feireira, V.G., Cuminato, J.A., Castelo, A. & Sousa, F.S. & Mangiacavacchi, N., The MAC method. *Computers & Fluids*, **37**, pp. 907–930, 2008. <https://doi.org/10.1016/j.compfluid.2007.10.006>
- [6] Lemos, C., Higher-order schemes for free surface flows with arbitrary configurations. *International Journal of Numerical Methods in Fluids*, **23**, pp. 545–566, 1996. [https://doi.org/10.1002/\(sici\)1097-0363\(19960930\)23:6<545::aid-fld440>3.0.co;2-r](https://doi.org/10.1002/(sici)1097-0363(19960930)23:6<545::aid-fld440>3.0.co;2-r)
- [7] Sussman, M., Smereka, P. & Osher, S.J., A level set approach for computing solutions to incompressible two-phase flow. *Journal of Computational Physics*, **114**(1), pp. 146–159, 1994. <https://doi.org/10.1006/jcph.1994.1155>
- [8] Unverdi, S.H. & Tryggvason, G., A front-tracking method for viscous, incompressible, multi-fluid flows. *Journal of Computational Physics*, **100**(1), pp. 25–37, 1992. [https://doi.org/10.1016/0021-9991\(92\)90307-k](https://doi.org/10.1016/0021-9991(92)90307-k)
- [9] Tryggvason, G., Bunner, B., Esmaeeli, A., Juric, D., Al-Rawahi, N., Tauber W., Han, J., Nas, S. & Jan, Y.J., A front-tracking method for the computations of multiphase flow. *Journal of Computational Physics*, **169**, pp. 708–759, 2001. <https://doi.org/10.1006/jcph.2001.6726>
- [10] Razi, M. & Pourghasemi, M., Direct numerical simulation of deformable droplets motion with uncertain physical properties in macro and micro channels. *Computer & Fluids*, **154**(1), pp. 200–210, 2017. <https://doi.org/10.1016/j.compfluid.2017.06.005>

- [11] Ingber, M.S., Combined static and hydrodynamic interactions of two rough spheres in nonlinear shear flow. *Journal of Rheology*, **54**(4), 707–718, 2010. <https://doi.org/10.1122/1.3429067>
- [12] Ingber, M.S. & Zinchenko, A., Semi-analytic solution of the motion of two spheres in arbitrary shear flow. *International Journal of Multiphase Flow*, **42**, pp. 152–163, 2012. <https://doi.org/10.1016/j.ijmultiphaseflow.2012.01.005>
- [13] Fathi, N., Ingber, M., & Vorobieff, P. Particle interaction in oscillatory Couette and Poiseuille flows. *Bulletin of the American Physical Society*, **58**, 2013.
- [14] Fathi, N., Ingber, M., & Vorobieff, P., Particle behavior in linear shear flow: An experimental and numerical study. *Bulletin of the American Physical Society*, **57**, 2012.
- [15] Fathi, N. & Vorobieff, P., *Spherical Particles in a Low Reynolds Number Flow: A V&V Exercise*. ASME Verification and Validation Symposium, 2013.
- [16] Pourghasemi, M., Fathi, N., Vorobieff, P., Ahmadi, G. & Kevin, R., Anderson. Multiphase flow development on single particle migration in low Reynolds number fluid domains. In *Fluids Engineering Division Summer Meeting*, vol. 83723, p. V002T04A038. American Society of Mechanical Engineers, 2020.
- [17] Vorobieff, P., Fathi, N., Aleyasin, S. S. & Ahmadi, G., Transport of a single spherical particle in low Reynolds numbers' linear shear flows: Experiment and modeling. *WIT Transactions on Engineering Sciences*, **128**, pp. 69–76, 2020.
- [18] Nakayama, Y., Kim, K. & Yamamoto, R., Simulating (electro) hydrodynamic effects in colloidal dispersions: Smoothed profile method. *The European Physical Journal E*, **26**(4), pp. 364–368, 2008. <https://doi.org/10.1140/epje/i2007-10332-y>
- [19] Nakayama, Y. & Yamamoto, R., Simulation method to resolve hydrodynamic interactions in colloidal dispersion. *Physical Review E*, **71**, 2006. 036707-1-036707-7
- [20] Chorin, A.R., Numerical solution of the Navier–Stokes equations. *Mathematics of Computation*, **22**, p. 745, 1968. <https://doi.org/10.1090/s0025-5718-1968-0242392-2>
- [21] Saffman, P.G.T., The lift on a small sphere in a slow shear flow. *Journal of Fluid Mechanics*, **22**(2), pp. 385–400, 1965. <https://doi.org/10.1017/s0022112065000824>